magnetochemistry

MDPI

Article

Bifunctional Magnetite–Gold Nanoparticles for Magneto-Mechanical Actuation and Cancer Cell Destruction

Anastasiia S. Garanina [1,*,†], Maria V. Efremova [1,2,3,†], Alexey E. Machulkin [3,4], Evgeny V. Lyubin [5], Natalia S. Vorobyeva [1], Oxana A. Zhironkina [6], Olga S. Strelkova [6], Igor I. Kireev [6], Irina B. Alieva [6], Rustem E. Uzbekov [7,8], Viatcheslav N. Agafonov [9], Igor V. Shchetinin [1], Andrey A. Fedyanin [5], Alexander S. Erofeev [1,3], Peter V. Gorelkin [10], Yuri E. Korchev [1,11], Alexander G. Savchenko [1] and Maxim A. Abakumov [1,12]

1 National University of Science and Technology «MISiS», Moscow 119049, Russia
2 Department of Applied Physics and Science Education, Eindhoven University of Technology, 5600 MB Eindhoven, The Netherlands
3 Department of Chemistry, Lomonosov Moscow State University, Moscow 119991, Russia
4 Biochemistry Department, RUDN University, Moscow 117198, Russia
5 Department of Physics, Lomonosov Moscow State University, Moscow 119991, Russia
6 Belozersky Institute of Physico-Chemical Biology, Lomonosov Moscow State University, Moscow 119992, Russia
7 Faculté de Médecine, Université François Rabelais, 37200 Tours, France
8 Department of Bioengineering and Bioinformatics, Lomonosov Moscow State University, Moscow 119234, Russia
9 GREMAN, UMR CNRS 7347, Université François Rabelais, 37200 Tours, France
10 Medical Nanotechnology LLC, Skolkovo Innovation Center, Moscow 121205, Russia
11 Faculty of Medicine, Imperial College London, London SW7 2AZ, UK
12 Department of Medical Nanobiotechnology, Russian National Research Medical University, Moscow 117997, Russia
* Correspondence: anastasiacit@gmail.com
† These authors contributed equally to this work.

Abstract: Magnetite–gold dumbbell nanoparticles are essential for biomedical applications due to the presence of two surfaces with different chemical natures and the potential combination of magnetic and plasmonic properties. Here, the remote actuation of Fe_3O_4-Au hybrid particles in a rotating (1 Hz, 7 mT), static (7 mT) or pulsed low-frequency (31 Hz, 175 mT, 30 s pulse/30 s pause) magnetic field was studied. The particles were synthesized by a high-temperature wet chemistry protocol and exhibited superparamagnetic properties with the saturation magnetization of 67.9 ± 3.0 Am^2 kg^{-1}. We showcased the nanoparticles' controlled aggregation in chains (rotating/static magnetic field) in an aqueous solution and their disaggregation when the field was removed. The investigation of nanoparticle uptake by LNCaP and PC-3 cancer cells demonstrated that Fe_3O_4-Au hybrids mainly escaped endosomes and accumulated in the cytoplasm. A significant fraction of them still responded to a rotating magnetic field, forming short chains. The particles were not toxic to cells at concentrations up to 210 μg (Fe_3O_4) mL^{-1}. However, cell viability decrease after incubation with the nanoparticles ($\geq$70 μg mL^{-1}) and exposure to a pulsed low-frequency magnetic field was found. We ascribe this effect to mechanically induced cell destruction. Overall, this makes Fe_3O_4-Au nanostructures promising candidates for intracellular actuation for future magneto-mechanical cancer therapies.

Keywords: magnetite–gold dumbbell nanoparticles; low-frequency magnetic field; biomedical application; prostate cancer cells; cancer cell destruction; SICM

check for updates

Citation: Garanina, A.S.; Efremova, M.V.; Machulkin, A.E.; Lyubin, E.V.; Vorobyeva, N.S.; Zhironkina, O.A.; Strelkova, O.S.; Kireev, I.I.; Alieva, I.B.; Uzbekov, R.E.; et al. Bifunctional Magnetite–Gold Nanoparticles for Magneto-Mechanical Actuation and Cancer Cell Destruction. *Magnetochemistry* **2022**, *8*, 185. https://doi.org/10.3390/magnetochemistry8120185

Academic Editor: Andrea Caneschi

Received: 4 November 2022
Accepted: 7 December 2022
Published: 12 December 2022

Publisher's Note: MDPI stays neutral with regard to jurisdictional claims in published maps and institutional affiliations.

Copyright: © 2022 by the authors. Licensee MDPI, Basel, Switzerland. This article is an open access article distributed under the terms and conditions of the Creative Commons Attribution (CC BY) license (https://creativecommons.org/licenses/by/4.0/).

1. Introduction

The development of nanotechnologies and their application in biomedicine has become one of the top research areas in recent decades. To date, a vast number of nanoparticles (NPs)

have been developed with various chemical compositions, sizes, shapes, and modifications designed to perform specific aims. Magnetic NPs (MNPs) are of the most significant interest, since their application in medicine is highly diverse and dominant. MNPs are actively used as contrast agents to improve the efficiency of diagnostics by magnetic resonance imaging (MRI) [1,2]. They act as converters of electromagnetic energy into heat energy under high-frequency alternating magnetic field exposure during therapy with hyperthermia [3]. MNPs can be used to remotely monitor different molecules and processes at the nanoscale level under low-frequency magnetic field exposure. In particular, they are proposed to be applied for the separation and purification of biological molecules and cells [4], as well as for gene expression regulation and the activation of various signaling cascades in the cell [5]. Additionally, in cancer therapy MNPs can act as drug carriers, facilitating their accumulation and release in the tumor under an external magnetic field exposure [6,7]. Moreover, special attention has recently been paid to the MNP application to activate tumor cell death due to the magneto-mechanical effect [8–10]. It consists of the fact that MNPs exposed to a low-frequency magnetic field undergo mechanical movements to align their magnetic moments to the field directions. Such movements generate mechanical forces, affecting cellular structures close to the MNPs [9]. As a result, the magneto-mechanical effect can induce different cell death signaling pathways leading to apoptosis and necrosis [8,11]. Mechanisms underlying cell death depend on whether MNPs interact with the cell membrane, cytoplasm, cytoskeleton, nucleus or lysosomes [12].

One of the critical factors affecting the efficiency of the magneto-mechanical impact on tumor cell destruction is a selection of optimal magnetic field parameters [8]. This topic is discussed in numerous experimental works, and the data obtained do not always agree with but sometimes contradict each other. A pulsed low-frequency magnetic field was shown to decrease cell viability by up to 70%, while static and rotating fields were less effective [13], wherein the rotating field was more efficient than the alternating field [8]. The amplitude of the applied magnetic field is also crucial for tumor cell death activation. Li et al. demonstrated that in the range of 0.1–20 mT, a magnetic field with higher amplitude caused an increased cell death rate [14]. On the other hand, Lopez et al. found that cell exposure to a magnetic field with an amplitude of about 40 mT resulted in more pronounced cell death than the field with a 100 mT amplitude [8]. However, Master et al. showed that the magnetic field amplitudes of 62 and 125 mT had the same effect on cell viability [15]. Moreover, the frequency of the magnetic field is being discussed as well. Wong et al. revealed that a higher number of apoptotic cells was observed at low frequencies of 1–5 Hz [16]. On the contrary, Li et al. found that an increasing magnetic field frequency in the range of 0–20 Hz caused enhanced cell death [14]. Chiriac et al. demonstrated that the most significant tumor cell viability decrease was observed in the frequency range of 20–50 Hz [17].

Finally, different types of MNPs, including their shape and size, are used for magneto-mechanical effect actuation. As for the chemical composition, MNPs can be Fe_3O_4, NiFe, Ni, iron oxide doped with zinc, iron carbide, and a lot of others; for the shape, spheres, cubes, rods, discs, wires, etc.; and for the size, from 6 nm to 2 μm [18–21]. Various surface modifications are applied to increase MNP delivery to tumor cells or specific organelles. Zhang et al. coated MNPs with antibodies against LAMP-1 (lysosomal-associated membrane protein) that increased NP internalization by lysosomes [22]. Vegerhof et al. conjugated NPs with the antibody to EGF receptors, which is expressed at high levels by various epithelial tumors. This resulted in efficient tumor growth slowdown [23].

Thus, there is a large amount of data regarding the application of MNPs under low-frequency magnetic field exposure for magneto-mechanical effect actuation and cancer cell death activation. Nevertheless, to the best of our knowledge, the direct visualization of MNP behavior in solution and, furthermore, in living cells during magnetic field application is missing. In this study, magnetite–gold dumbbell nanoparticles, with magnetite epitaxially grown on gold seeds (i.e., Fe_3O_4 and Au nanoparticles are pairwise connected in the final hybrid structure) were investigated. They have already proven to be used as a contrast agent for MRI [24], to provide controlled magnetic hyperthermia [25], and to

ensure drug delivery, including targeted delivery [24,26]. Here, their effectiveness for magneto-mechanical actuation and cancer cell destruction was studied. MNP interaction and accumulation in tumor cells, as well as their impact for cell death induction under pulsed low-frequency magnetic field exposure, were analyzed. Moreover, the MNPs' behavior under different types of magnetic fields (rotating, alternating current or constant) was visualized in real time.

2. Materials and Methods

2.1. Synthesis of Magnetic Nanoparticles

The 1-octadecene, oleic acid, oleylamine, 1,2-hexadecanediol, iron pentacarbonyl, gold (III) chloride hydrate, (3-Aminopropyl)triethoxysilane (APTES), dimethyl sulfoxide (DMSO) were purchased from Sigma-Aldrich. Isopropanol, acetic acid, and toluene were purchased from Reachim. Sulfo-Cyanine5 NHS ester was delivered by Lumiprobe. Dialysis bags (MWCO 12 kDa) were purchased from Spectrum Laboratories, Inc (Rancho Dominguez, CA, USA).

The synthesis of Fe_3O_4-Au dumbbell MNPs was performed as described in [27]. Briefly, 1-octadecene (100 mL), oleic acid (10 mL), oleylamine (10 mL), and 1,2-hexadecanediol (6.44 g) were mixed on a magnetic stirrer in a three-neck round-bottom flask and heated to 120 °C under argon atmosphere for 20 min. Then, iron pentacarbonyl (1.5 mL) was injected into the obtained mixture along with hydrogen tetrachloroaurate (150 mg) dispersed in 1-octadecene (12.5 mL) and oleylamine (1.25 mL). The reaction mixture was heated under reflux (310 °C) for 45 min; after that, it was cooled down to room temperature and air-exposed for 1 h. The obtained MNPs were isolated by adding isopropanol with subsequent centrifugation (6000 rpm, 10 min) and dried in a vacuum.

To introduce amino groups onto the MNP surface, they were coated with APTES. For this purpose, 100 mL APTES and 50 µL acetic acid were added to 10 mg of MNPs dispersed in 10 mL of toluene. The mixture was heated to 40 °C and mixed overnight. Afterwards, APTES-coated MNPs with amino groups on the surface were precipitated with a permanent magnet, washed with deionized water several times, and redispersed in 9 mL of 0.1M PBS (pH = 8.3) according to the protocol of the manufacturer. Then, APTES-coated MNPs were mixed with a solution of Sulfo-Cyanine5 NHS ester dye in 1 mL DMSO according to the protocol of the manufacturer and mixed at room temperature overnight. Fluorescently labeled APTES-coated MNPs (MNPs-Cy5) were purified from the excess of a Cy5 dye by multiple centrifugations, and then the resulting MNPs-Cy5 solution was dialyzed against deionized water (MWCO 12 kDa) for 24 h with a final pH = 7.0. This solution was used for the transmission electron microscopy and dynamic light scattering measurements as well as for all experiments in a magneto-optical system (with or without cells). For the X-ray diffraction and magnetic property measurements, we used the powder obtained by drying the sample of MNPs (i.e., before coating with APTES) in a vacuum.

2.2. Transmission Electron Microscopy (TEM)

For TEM analysis, 3 µL of MNPs-Cy5 solution was placed on the grid with formvar films for 1 min. Then, water was removed with filter paper, and the sample was left to dry. JEM-2100F/Cs transmission electron microscope (JEOL) was used to analyze the obtained sample. The average diameter of MNPs was calculated from TEM images by analyzing 500 NPs using Image J software (National Institutes of Health, Bethesda, MD, USA).

2.3. Dynamic Light Scattering (DLS) Measurements

The hydrodynamic size and zeta potential of MNPs-Cy5 in deionized water were measured at 25 °C by DLS using a Nano ZS ZetaSizer (Malvern Instruments). The average particle sizes with error ranges were obtained from three independent measurements.

2.4. X-ray Diffraction (XRD)

XRD patterns of MNPs were obtained using an X-ray powder diffractometer DRON-4 with CoKα radiation. The data were collected from 2θ = 20 to 140° at a scan rate of 0.1° per step and 3 s per point. Qualitative phase analysis was performed by comparison of the obtained spectra with the ICDD PDF-2 database. Qualitative and quantitative phase analysis was carried out using the PDXL software product (Rigaku, Japan) together with the ICCD PDF-2 database. Quantitative phase analysis was carried out by the Rietveld method implemented in the PDXL software product by means of full-profile fitting of the calculated and experimental spectra. For fitting the spectra, the lattice parameters, the amount of each phase and their crystallite diameter were optimized.

2.5. Analysis of MNP Magnetic Properties

M-H hysteresis loops of MNPs (from −3 to 3 T, 300 K) were obtained on the «Quantum Design» Physical Property Measurement System (PPMS) equipped with a vibration magnetometric device (VSM) with 2 mm amplitude of oscillations and 40 Hz frequency. Moreover, the MNP solution was examined by a magneto-optic system [28,29]. For this purpose, the solution of MNPs-Cy5 in distilled water (≈200 µL; 30 µg mL^{-1} Fe_3O_4, 5 µg mL^{-1} Au, 1 µg mL^{-1} Cy5) was placed on the cover glass #0 (thickness 0.08–0.13 mm, Boreal) and covered by another glass. Both glasses were pre-treated with hydrogen peroxide. This chamber was sealed with petrolatum and placed on the objective table of the magneto-optic system. Three types of magnetic fields were applied: rotating (1 Hz, 7 mT), static (7 mT), and alternating current field (1 Hz, 7 mT). Videos were taken with an acquisition rate of 15 frames/s using CMOS Color Camera Thorlabs DCC1645C, 1280 × 1024, and Thorlabs uc480 Viewer software.

2.6. Cell Lines

LNCaP and PC-3 human prostate cancer cells were purchased from the American Type Culture Collection (ATCC, Manassas, VA, USA). Cells were maintained in RPMI-1640 medium (gibco) supplemented with 10% Fetal Bovine Serum (Sigma), 2 mM L-glutamine, antibiotics (0.1 U mL^{-1} penicillin and 0.1 µg mL^{-1} streptomycin; gibco), and RPMI vitamin solution (Sigma). Cells were cultured at 37 °C in a humidified incubator (Sanyo) supplied with 5% CO_2. Cells were seeded on glass coverslips or in 96-well plates (Corning) at concentrations 120,000 cells per mL for LNCaP and 70,000 cells per mL for PC-3 in experiments. The counting of cells was carried out using automatic cell counter MOXI.

2.7. Cell Incubation with MNPs

Two days after cell seeding, the solution of ultrasound pre-treated MNPs-Cy5 in H_2O_d was added to the culture medium at 30 µg mL^{-1} Fe_3O_4, 5 µg mL^{-1} Au, and 1 µg mL^{-1} Cy5 concentrations. Cells were incubated with MNPs-Cy5 for different durations depending on the experiment.

2.8. Dynamic of MNPs-Cy5 Accumulation in Cells

Cells were incubated with MNPs-Cy5 for 45 min, 2, 6, and 24 h and fixed with 3.7% formaldehyde (Sigma) (on PBS) for 15 min. Cell nuclei were stained with DAPI (Sigma) for 10 min. The obtained preparations were imaged using an inverted fluorescence microscope EVOS (life technologies, objective PlanFluor 60×/0.75).

2.9. Immunofluorescent Staining

After 2 h of incubation with MNPs-Cy5, cells were fixed as described previously, permeabilized with 0.2% Triton X-100 (AppliChem) in PBS for 5 min, and incubated in PBS supplemented with 1% BSA for 1 h. The primary antibodies were rabbit anti-β-catenin antibody (Sigma, 1:1000) and rabbit polyclonal anti-LAMP1 antibody (abcam, 1:100). Alexa Fluor 568 donkey anti-rabbit IgG (Invitrogen, 1:800) and Alexa Fluor 488 goat anti-rabbit IgG (Invitrogen, 1:800) were used as secondary antibodies. DNA was stained with DAPI.

The samples were analyzed using an EVOS microscope and an inverted laser scanning confocal microscope Nikon C2 with a black-and-white camera Andor iXon, Plan Apo 40×/0.95 objective, and NIS-Elements AR 4.13 application. The further processing of the photos was carried out by ImageJ software.

2.10. Scanning Surface Confocal Microscopy (SSCM)

Cells were seeded in Petri dishes with a glass bottom preliminarily covered with poly-L-lysine (Sigma) for 1 h. After 2 h incubation with MNPs-Cy5, cells were washed with HBSS (gibco) containing 10 mM HEPES (helicon) and 1% of Glutamax (gibco). The pH of the solution was adjusted to 7.4 with 1N sodium hydroxide (NaOH). The basic arrangement of the scanning ion-conductance microscope (SICM) for topographical imaging was previously described in [30,31]. SSCM, which is the combination of SICM and scanning confocal microscopy (SCM), was reported by Gorelik et al. [32].

The nanopipettes for the study using SSCM were made from borosilicate glass with filament (outer diameter—1.00 mm; inner diameter—0.50 mm (Intracel, Herts, UK)) on a laser-based Brown-Flaming puller (model P-2000, Sutter Instrument Company, San Rafael, CA). The nanopipettes were filled with modified HBSS. The measured nanopipette resistance was ≈130 MΩ. To perform simultaneous scanning laser confocal microscopy and SICM, an LCSDTL-364 laser diode (647 nm wavelength, Laser Compact, Moscow, Russia) was used. The optical recording system consisted of a Nikon Diaphot inverted microscope (Diaphot 200, Nikon Corporation, Tokyo, Japan) equipped with an oil-immersion objective lOOX 1.3 NA, an epifluorescent filter block and a photomultiplier with a pinhole (D-104–814, Photon Technology International, Surbiton, England). The laser was focused onto the top surface of the coverslip and combined with the nanopipette tip raised above the surface. The position of the pipette was noted on the camera monitor, and the pipette was then positioned to appear at this point on the monitor before any experiment. This was a reproducible way to position the pipette in the XY direction and the laser focus.

The obtained images were processed and analyzed using SICM Image Viewer software.

2.11. Correlative Light-Electron Microscopy (CLEM)

After 2 h incubation of cells with MNPs-Cy5, they were fixed in 2.5% glutaraldehyde with 2% formaldehyde in 0.1 M phosphate buffer (pH 7.4). The time of fixation was 1 h. DNA was stained with DAPI. After fluorescent images were taken, the same cells were marked under DIC (differential interference contrast) (Nikon C2, Plan Apo 20×/0.75 and 10×/0.3). The cell layer around the marked area was brushed off using a fine needle, and after this the samples were subjected to a TEM procedure.

2.12. Transmission Electron Microscopy of Cells

For TEM analysis of cells, a standard protocol described in [26] was used. Ultrathin (70 nm) sections were made using a diamond knife and examined under a JEM-1400 transmission electron microscope (JEOL) at an accelerating voltage of 100 kV.

2.13. Cytotoxicity Assay of MNPs-Cy5

Two days after cell seeding in 96-well plates, serial dilutions of MNPs-Cy5 in H_2O_d were added to cells. Cells incubated in a culture medium were used as a control. Distilled water was used as a negative control, while 20% DMSO diluted in the cell medium was used as a positive control. Cells were incubated for 48 h at 37 °C and 5% CO_2. Later, the culture medium from each well was removed, and 20 µL of MTS reagent (CellTiter 96 AQueous Non-Radioactive Cell Proliferation Assay, Promega) were added to each well with 100 µL of new culture medium. After 4 h incubation at 37 °C in darkness, plates with cells were placed on a permanent magnet for 3–5 min to remove the MNPs-Cy5 from the solution, and 100 µL of the medium with MTS from each well were carefully replaced in new plates. The absorbance of the obtained solution was measured at 490 nm wavelength using a Thermo Scientific Multiskan GO spectrometer. Cell viability was calculated as a

percent compared to cells incubated in a culture medium. The MTS assay revealed 100% cell death after incubation with 20% DMSO (data not shown). The absorbance of the MTS reagent in a culture medium without cells was taken as zero. Experiments were performed in triplicate.

2.14. MNPs-Cy5 Behavior inside Cells under Low-Frequency Magnetic Field Exposure

Cells seeded on glass #0 were incubated with MNPs-Cy5 for 24 h, embedded in the camera described above, and placed in a magneto-optic system. A rotation field with parameters f = 1 Hz and B = 7 mT was applied, and videos were taken as previously described.

2.15. MNPs-Cy5 Effect on Cells under Low-Frequency Magnetic Field Exposure

Serial dilutions of MNPs-Cy5 in H_2O_d were added to cells seeded in 96-well plates. Cells incubated in a complete culture medium or medium with the addition of H_2O_d were used as controls. Plates were placed in alternating magnetic field generator TOR Ultra (NanoMaterials, Russia) for 3 h, maintaining room temperature. A pulsed magnetic field with parameters f = 31 Hz and B = 175 mT was applied by cycles of 30 s pulse–30 s pause. Similar plates incubated at room temperature in the darkness without magnetic field exposure were used as a control. Later, a cytotoxicity assay was performed, as described above.

2.16. Statistical Analysis

Data were analyzed using the unpaired *t*-test in GraphPad Prism 9 software. *p*-values < 0.05 were considered significant.

3. Results

3.1. Magnetite–Gold Dumbbell Nanoparticle Characterization and Magnetic Properties

The transmission electron microscopy (TEM) analysis of synthesized magnetite–gold dumbbell nanoparticles (MNPs) labeled with fluorescent Cy5 dye (MNPs-Cy5) revealed that the magnetite (Fe_3O_4) had an irregular shape close to a spherical one and a mean diameter of 21 ± 3 nm, while the gold (Au) NPs were spheres with 3 ± 1 nm diameter (Figure 1a–c).

Figure 1d,e show the hysteresis loop of MNPs at 300 K with a saturation magnetization Ms = 67.9 ± 3.0 $Am^2\ kg^{-1}$ (Fe_3O_4) and a coercive field μ_0H_C = 1.1 ± 1.0 mT. Therefore, at room temperature the synthesized MNPs-Cy5 can be considered superparamagnetic. According to the DLS measurements, the MNPs had a hydrodynamic diameter of 251 ± 23 nm (at pH 7.0), which means that they existed in solution as conglomerates of ~a hundred individual MNPs. The zeta potential of the MNPs was positive (the value of 15 ± 4 mV at pH 7.0) due to the presence of amino groups on the MNPs' surface from the APTES coating.

The qualitative and quantitative phase composition of MNPs was investigated by X-ray diffraction (XRD). The experimental data are presented in Figure S1, where all the expected peaks of magnetite and gold can be observed. The Rietveld refinement, combining the powder diffraction reference data of Fe_3O_4 (ICDD PDF-2 No. 00-019-0629) and Au (ICDD PDF-2 No. 03-065-8601), was applied. The extracted lattice constants, crystallite size and phase volume fractions are listed in Table S1. In particular, we found the volume fractions of the phases to be 96.0% (Fe_3O_4) and 4.0% (Au). Considering the MNPs' density of 5.0 g cm^{-3} (Fe_3O_4) and 19.3 g cm^{-3} (Au), mass fractions of Fe_3O_4 and Au equal to 86.1% (Fe_3O_4) and 13.9% (Au) were calculated. This is in line with previous reports on Fe_3O_4-Au hybrid particles of similar size and the estimation of Fe_3O_4/Au volume fractions from the average MNP diameter according to the TEM [25].

Since magnetite (Fe_3O_4) and maghemite (γ-Fe_2O_3) are structurally similar, XRD alone does not provide an accurate discrimination between the two phases [33]. As listed in Table S1, the lattice parameter of the iron oxide phase in the MNP sample (a = 0.8363) is an intermediate value between bulk Fe_3O_4 (a = 0.8397 nm) and bulk γ-Fe_2O_3 (a = 0.8347 nm). Interestingly, while Au NPs are single-crystalline (XRD crystallite diameter = 3.0 nm, TEM diam-

eter = 3 ± 1 nm), Fe_3O_4 NPs appear to be polycrystalline (crystallite diameter = 12.0 nm, average TEM diameter = 21 ± 3 nm).

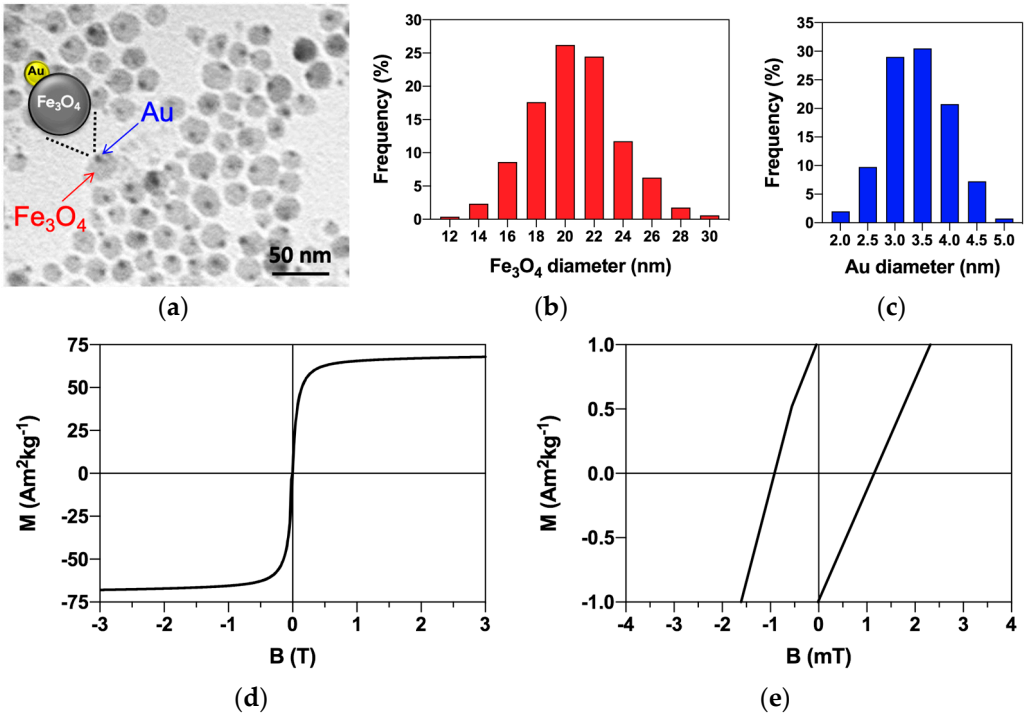

Figure 1. Magnetite–gold dumbbell nanoparticle characterization. (**a**) TEM micrograph of investigated MNPs-Cy5 with the schematical representation of the nanoparticle structure; (**b**) Histogram of magnetite size distribution obtained from the analysis of TEM micrographs; (**c**) Histogram of gold size distribution obtained from the analysis of TEM micrographs; (**d**) Hysteresis loop of MNPs at 300 K, VSM; (**e**) Close-up of a hysteresis loop demonstrating a coercive field of MNPs at 300 K.

To visualize the behavior and a real-time movement of MNPs-Cy5 in water solution (used for all in vitro experiments) under a low-frequency magnetic field, they were placed into a magneto-optic system. Chaotically located MNP conglomerates with a size ≤1 μm (in agreement with the DLS measurements) undergoing a Brownian motion were detected before the magnetic field application (Figure 2a, Video S1).

Such conglomerates became magnetically attracted to each other and formed chains of 3–7 μm in length during 16 s exposure to a rotation field with parameters f = 1 Hz and B = 7 mT (Figure 2b–d, Video S2). These chains rotated with a frequency of one turnover per second, i.e., with the frequency of the applied magnetic field. After the rotation field was changed to the constant field, previously formed chains of MNP-Cy5 conglomerates lined up along the magnetic field lines (Figure 2e), and separate chains were attracted to each other (Figure 2f–h, Video S3). As a result, new longer chains (about 30 μm) were formed (in ≈32 s). The application of an alternating current field to the diffusely located MNP-Cy5 conglomerates led to the formation of long chains (10–20 μm) lined up along the field lines (Figure 2i). The termination of the magnetic field impact resulted in chain disintegration to individual MNP-Cy5 conglomerates, wherein such single conglomerates initially maintained a position close to that in the chain. Further, this chain became increasingly uneven, and after 2 s, we detected chaotically located MNP-Cy5 conglomerates (Figure 2j–l, Video S4).

Thus, synthesized MNPs-Cy5 can be assembled into linear aggregates (chains) in a time-controlled manner under an external magnetic field in a water solution and disassembled back to separate conglomerates as soon as the field is removed. Altogether, this provides an opportunity for real-time observations, aiming for MNPs-Cy5 and their chains as a magneto-mechanical tool for manipulating cells/organelles.

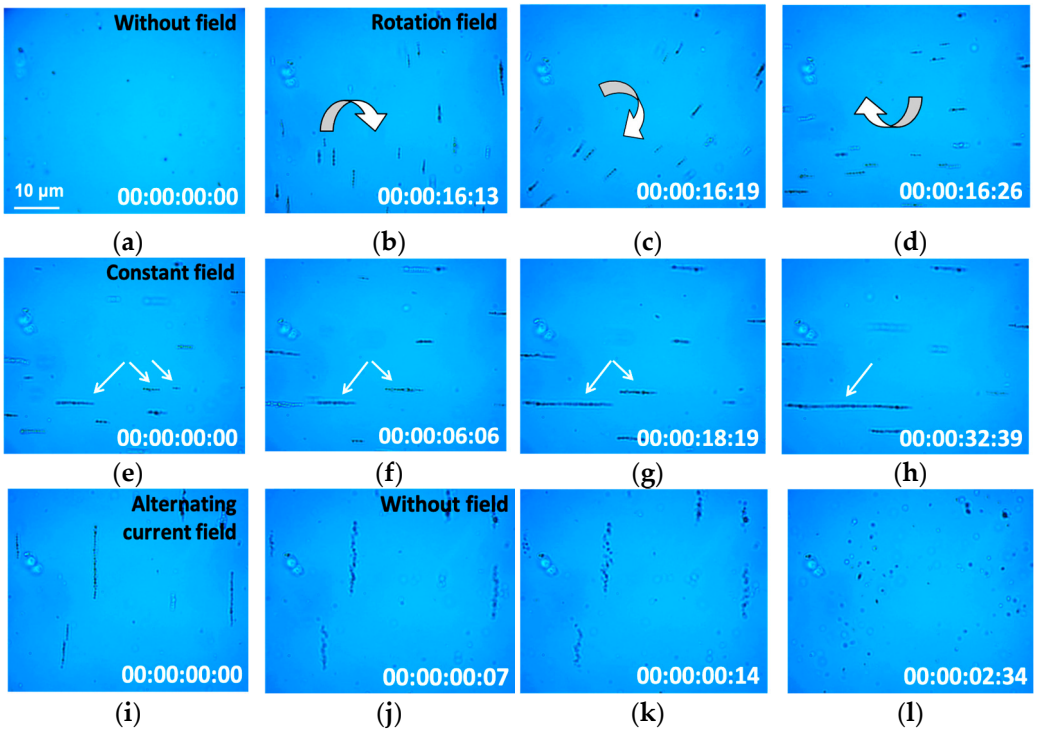

Figure 2. Magnetite–gold dumbbell nanoparticle behavior under low-frequency magnetic field in water solution. (**a**) MNPs before magnetic field exposure; (**b**–**d**) MNPs in rotation field (1 Hz, 7 mT); (**e**–**h**) MNPs in the constant field (7 mT); (**i**) MNPs in alternating current field (1 Hz, 7 mT); (**j**–**l**) MNPs after alternating current field termination.

3.2. Magnetic Nanoparticles Accumulation in Cells

To examine the dynamics of MNP accumulation in cells by fluorescent microscopy, we co-cultivated MNPs-Cy5 with LNCaP and PC-3 lines for various durations. After 45 min of co-incubation, no interaction of MNPs-Cy5 with the cells was detected (Figure 3a,e). However, 2 h of co-cultivation resulted in MNP localization both on the surface of the cell plasma membrane and inside the cell (Figures 3b,f and S2).

These data were confirmed by scanning surface confocal microscopy (SSCM), which allows us to simultaneously obtain an image of the object topography and detect the fluorescence signal in the scanned area at a high resolution. Thus, Figure 4a–c demonstrates the MNP-Cy5 conglomerate on the surface of the cell plasma membrane, while Figure 4d–f shows the signal from MNPs-Cy5, which is localized under the plasma membrane. Moreover, the intracellular MNP localization after 2 h of co-incubation with cells was demonstrated by correlative light-electron microscopy (CLEM). Two aggregates of MNPs-Cy5 are shown on the fluorescent micrograph in Figure S3, and the same conglomerates are present on the electron micrographs. Both are situated in the cell cytoplasm. As expected, the level of MNP uptake by prostate cancer cells was most noticeable after 24 h of co-cultivation (Figure 3d,h), while MNPs-Cy5 were internalized by LNCaP cells more often than by PC-3 cells. Thus, we can conclude that 2 h of co-incubation is enough for MNPs not only to interact with the cell plasma membrane but also to be inside the cell. Moreover, it was demonstrated that the two investigated tumor cell lines differ in endocytosis activity.

3.3. Magnetic Nanoparticles Uptake and Localization inside the Cell

While studying the MNP-Cy5 interaction with the cells, we obtained TEM images, which probably correspond to different stages of the MNPs' internalization. In the first stage, the cell forms pseudopodia surrounding the aggregate of MNPs (Figure 5a,b). Later, such a conglomerate entirely surrounded by the membrane was present inside the cell cytoplasm (Figure 5c). The TEM results also revealed the cases when aggregates of MNPs

were localized directly in the cell cytoplasm (Figure 5d,e) or inside double-membrane vacuoles, or autophagosomes (Figure 5f).

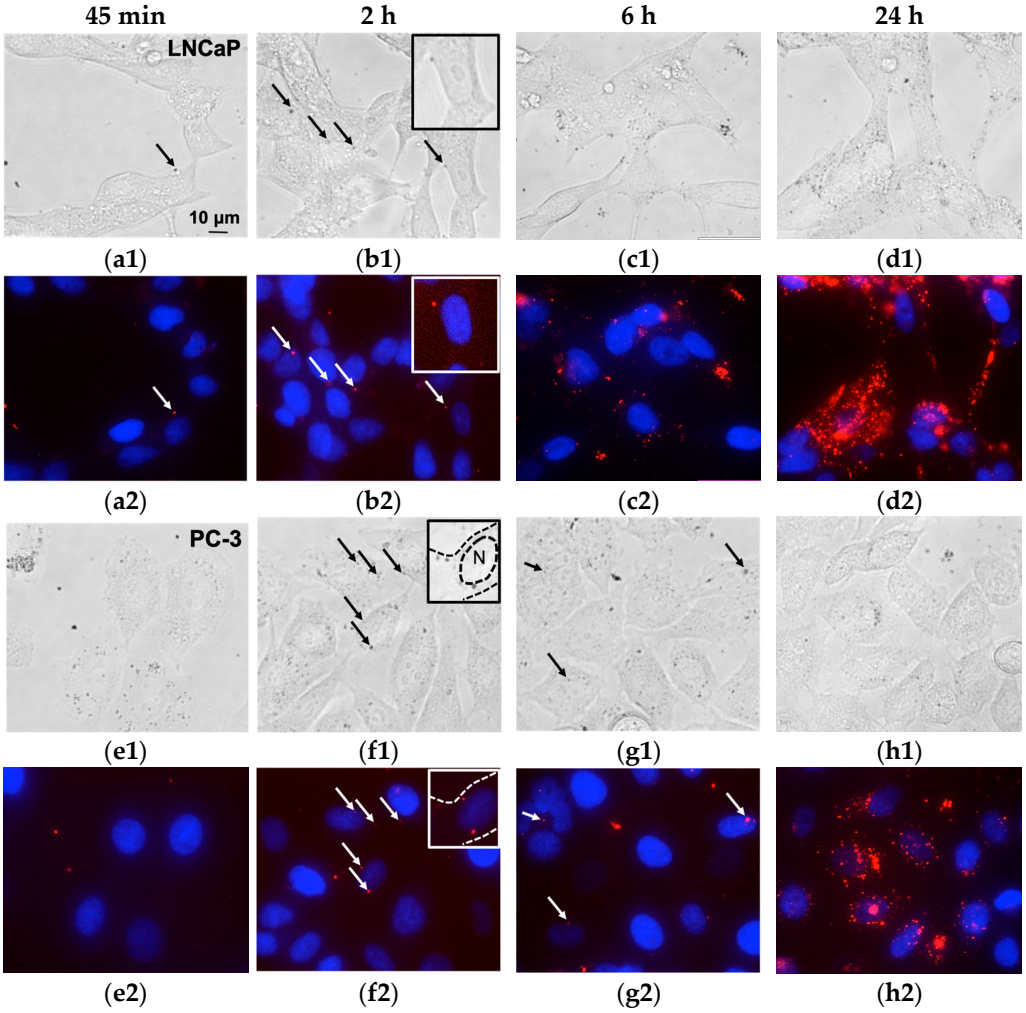

Figure 3. Dynamics of magnetite–gold dumbbell nanoparticles accumulation in cells. (**a**–**d**) MNP interaction with LNCaP cells after 45 min–24 h of co-incubation; (**e**–**h**) MNP interaction with PC-3 cells after 45 min–24 h of co-incubation. (**a1**–**d1**,**e1**–**h1**) Representative phase-contrast micrographs; (**a2**–**d2**,**e2**–**h2**) corresponding fluorescent micrographs: blue—cell nuclei stained with DAPI; red—MNPs labeled with Cy5. Arrows show some internalized MNPs. Dotted lines show the cell boundaries. Abbreviation: N—nucleus.

The staining of LNCaP and PC-3 cells with anti-LAMP1 (lysosomal-associated membrane protein 1) antibodies demonstrated that only single MNP-Cy5 conglomerates were located inside endolysosomes 2 h after co-incubation (Figures 5g,h, S4 and S5). However, most of the MNPs-Cy5 were not co-localized with an acidic vesicular cell compartment. The TEM investigation also demonstrated the predominant free localization of MNPs in the cell cytoplasm. Thus, we can conclude that synthesized magnetite–gold MNPs rapidly escape from the vesicle compartment after uptake, which delays their intracellular degradation and enhances the potential of MNPs-Cy5 for magneto-mechanical actuation in an external magnetic field.

3.4. Magnetic Nanoparticles Biocompatibility In Vitro

To define whether the MNP-Cy5 affect cell viability, we carried out the MTS assay. The results obtained for both investigated cell lines demonstrated that at concentrations up to 100 μg mL^{-1} (by Fe_3O_4), the MNPs did not cause a significant reduction in cell viability

(Figure 6a,b). A higher concentration of MNPs (210 μg mL^{-1}) resulted in an insignificant decrease in cell viability (about 25%), which may be due to the slightly positive charge of the MNP-Cy5 surface (according to the DLS data). Thus, we can conclude that the obtained MNPs-Cy5 are not toxic to cells.

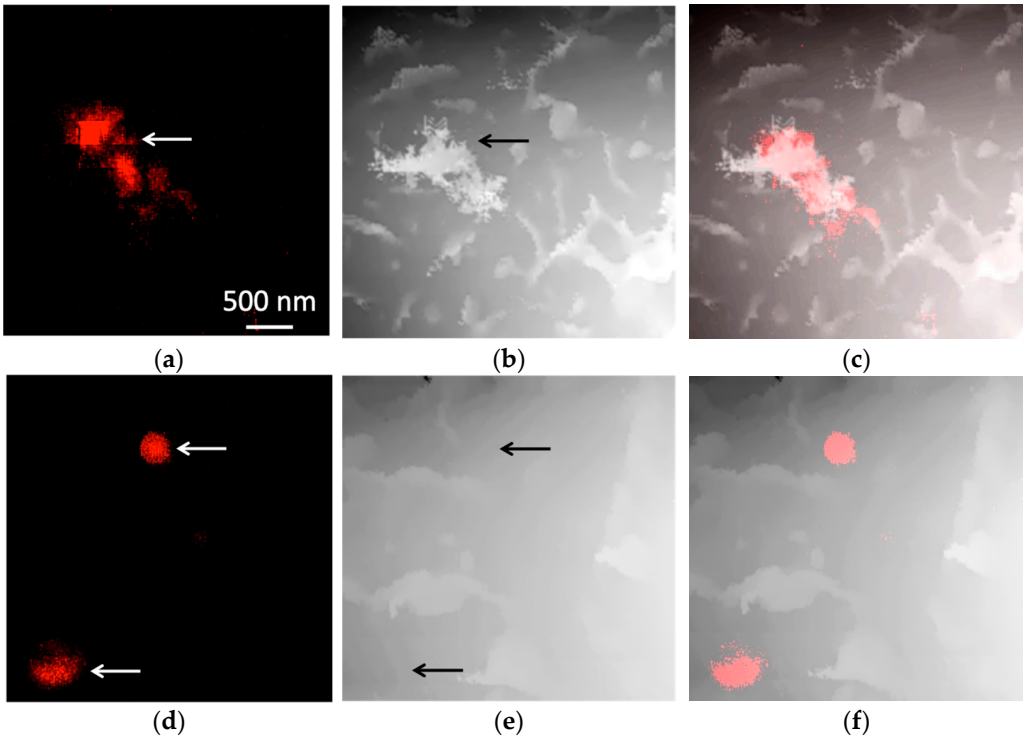

Figure 4. Magnetite–gold dumbbell nanoparticles interaction with cells. (**a**–**c**) MNP localization on the surface of cell plasma membrane; (**d**–**f**) MNP localization under the cell plasma membrane following their internalization. (**a**,**d**) Confocal laser scanning micrographs of MNPs modified with Cy5 dye; (**b**,**e**) topography micrographs of the same MNPs with cells, SICM; (**c**,**f**) merge of fluorescence and topography. Arrows show the MNPs of interest.

3.5. Magnetic Nanoparticle Impact on the Cells under Low-Frequency Magnetic Field Exposure

To investigate MNP behavior inside the cells under low-frequency magnetic field exposure, LNCaP and PC-3 cultures incubated with MNPs-Cy5 for 24 h were placed in a magneto-optic system. Small spherical-like conglomerates of MNPs were found inside the cells and near them. After the rotation field (1 Hz, 7 mT) was applied, some of these conglomerates began to move, similar to the previous experiment (in water), with the exact parameters of the magnetic field predominantly forming short chains or keeping the dispersed form (Figures S6 and S7, Videos S5–S7). Altogether, the type of MNP-Cy5 movement differed between their conglomerates: it could be rotational, oscillatory or indistinguishable. Notably, the rotation rate of the intracellular MNP-Cy5 conglomerates was not significantly different from the extracellular ones. Moreover, the detectable MNP conglomerates did not form long chains and rarely interacted with each other in the cell cytoplasm, as opposed to the experiments in water. It should be noted that the behavior of the internalized MNPs under magnetic field exposure was also dependent on the cell line. The observations mentioned above mainly concern the LNCaP cells. In the PC-3 cell line, the MNPs predominantly formed round-shaped conglomerates, only a few of which made rotational movements during the field application (Video S7), wherein the rotation rate of these conglomerates was somewhat lower than that of the extracellular ones. Interestingly, the MNPs' round-shaped conglomerate that rotated under magnetic field exposure in LNCaP cells stopped making these movements at a particular moment and began to move along the cell axis for a sufficiently large distance (Figure S8, Video S8).

We believe that this MNP conglomerate was captured and transported by microtubules at the moment of observation.

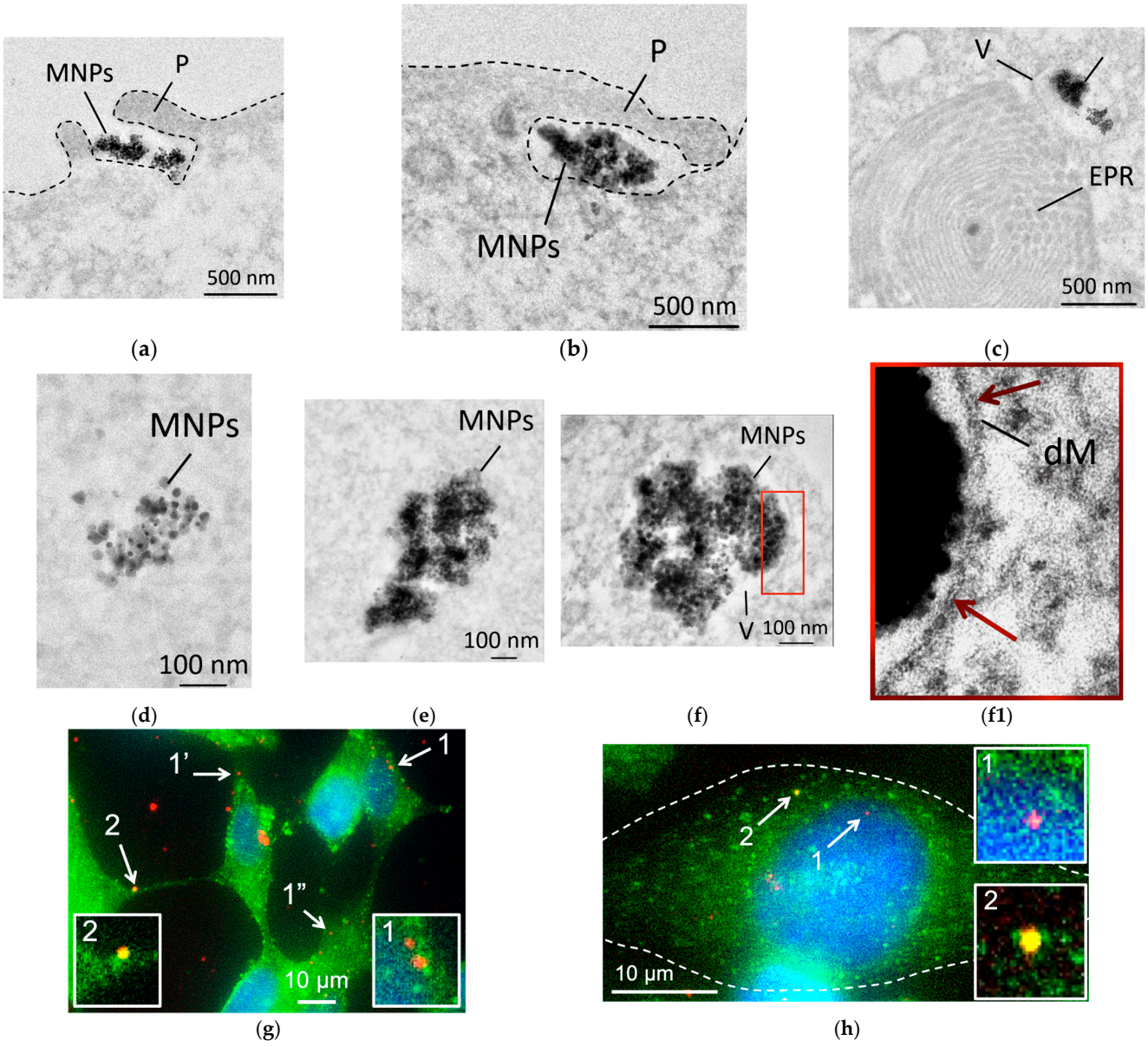

Figure 5. Magnetite–gold dumbbell nanoparticle internalization by cells and localization inside them. (**a**) Pseudopodia formation by cell; (**b**) Complete surrounding of MNP conglomerate by cell plasma membrane; (**c**) MNP localization inside cell vesicle; (**d**,**e**) Localization of MNP conglomerates with different sizes inside cell cytoplasm; (**f**) Location of MNP conglomerate inside double-membrane vacuole; (**f1**) Magnified view of the inset. Abbreviations: dM—double membrane; EPR—endoplasmic reticulum; MNPs—magnetic nanoparticles; P—pseudopodium formed by a cell plasma membrane; V—vesicle/vacuole. Arrows show the double membrane. Dotted lines indicate the cell boundaries. (**g**,**h**) Detection of MNP-Cy5 localization inside lysosomes in LNCaP and PC-3 cells, correspondingly. Fluorescent microscopy: green—cell vesicles stained with anti-LAMP1 antibodies, blue—cell nuclei stained with DAPI; red—MNPs labeled with Cy5. The 1, 1′ and 1″ show the MNP conglomerates, which are not situated inside the acidic vesicular compartment of the cells; 2—MNPs inside lysosome (Cy5 and anti-LAMP1 dye co-localization); frames 1 and 2—magnified views of corresponding areas; dotted lines indicate the cell boundaries.

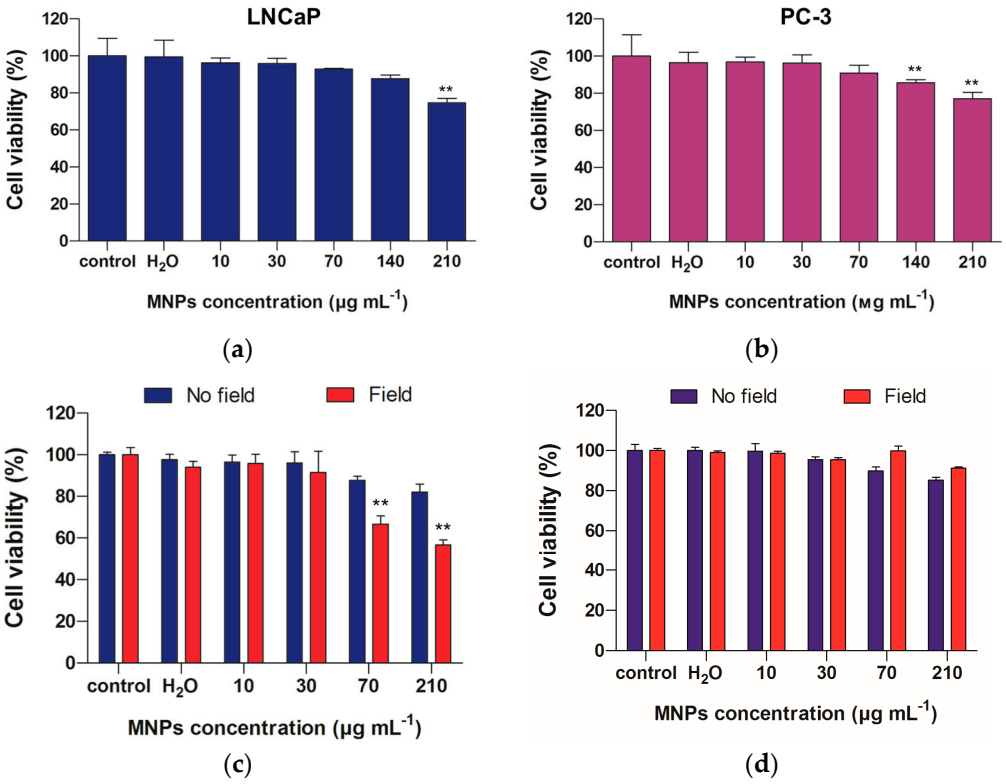

Figure 6. Magnetite–gold dumbbell nanoparticles' effect on cell viability. (**a**) Histogram of LNCaP cell survival after 48 h incubation with MNPs-Cy5; (**b**) Histogram of PC-3 cell survival after 48 h incubation with MNPs; (**c**) Histogram of LNCaP cell survival after 3 h incubation with MNPs under pulsed magnetic field exposure (f = 31 Hz and B = 175 mT, 30 s pulse–30 s pause) and without it; (**d**) Histogram of PC-3 cell survival after 3 h incubation with MNPs under pulsed magnetic field exposure and without it. MTS assay. ** $p < 0.05$ (*t*-test). In panels (**a**,**b**), the results were compared with control cells, and panels (**c**,**d**) with those without field application.

Thus, we demonstrated that MNP-Cy5 conglomerates partially retain magnetic properties even 24 h after the internalization by the cell and can accordingly respond to magnetic field exposure. In a magneto-optical setup, it was only possible to reach a 7 mT amplitude, which was a suitable field range for a proof-of-principle experiment on the real-time movement of MNPs-Cy5. To study their effect on the viability of tumor cells in an alternating magnetic field in vitro, another setup was used. The investigation of MNP-Cy5 impact on prostate cancer cells after 3 h of pulsed low-frequency magnetic field exposure (f = 31 Hz, B = 175 mT, 30 s pulse/30 s pause) revealed the decrease in cell viability in a dose-dependent manner for the LNCaP cell line (Figure 6c). Only high concentrations of MNPs-Cy5 ($\geq$70 μg mL^{-1} Fe_3O_4) resulted in pronounced cell death (>30%). However, magnetic field exposure did not lead to the death activation in the PC-3 culture co-incubated with MNPs-Cy5 at different concentrations (Figure 6d). Thus, the investigated MNPs have a magneto-mechanical effect on cells resulting in their death induction, but this effect depends on the NP concentration and specific cell line.

4. Discussion

The magneto-mechanical effect provided by MNPs under low-frequency magnetic field exposure is a growing field of research in biomedicine. It can be used in regenerative medicine and tissue engineering [34], in biomedicine for enzyme activity and cell receptor control, as well as for mechanically activated drug release [9,35], and in cancer therapy [21,36,37]. Different types of MNPs have been designed for specified purposes. In this article, we investigated the behavior and effectiveness of bifunctional magnetite–gold

NPs during low-frequency magnetic field application for tumor cell death activation. Such hybrid NPs have many advantages due to their biocompatibility [38], magnetic properties, and the presence of two surfaces, which can be modified [24,39,40]. Previously, we demonstrated that similar MNPs are well-established as contrast agents for MRI [24]. Moreover, subsequent studies have shown that magnetite–gold NPs with the same size (about 25 nm by TEM) enable effective controlled magnetic hyperthermia [25]. The presence of two surfaces, which enhances the variability of different modifications, makes these MNPs perfect candidates for application as targeted drug delivery platforms [24,26]. Finally, Fe_3O_4-Au MNPs are able to provide a synergistic effect of magnetic hyperthermia and photo-thermal/photodynamic therapy due to the potential combination of their magnetic and plasmonic properties given that the size ratio of both the Fe_3O_4 and Au components is tailored in the hybrid structure [24,41,42].

The investigation of the synthesized Fe_3O_4-Au MNPs' magnetic properties at room temperature revealed that the NPs could be considered superparamagnetic. This is in line with previous research on size-dependent properties of similar MNPs [25]. According to the magnetization curves (Figure 1d,e), in a 7 mT field, the magnetization of MNPs is 7 Am^2 kg^{-1}. Given that MNPs form conglomerates in a water solution or culture medium, the total magnetization per conglomerate is higher. Thus, MNPs-Cy5 respond to different types of low-frequency (rotating/alternating) and constant magnetic field in a magneto-optical system.

The synthesized magnetite–gold NPs were shown to be non-toxic to two human tumor cell lines (LNCaP and PC-3) at concentrations up to 70 μg (Fe_3O_4) mL^{-1}, causing a $\leq$25% decrease in cell viability at concentrations above 140 μg (Fe_3O_4) mL^{-1}. Moreover, it was revealed that the MNPs interacted with tumor cells (interaction with cell membranes was possibly enhanced due to the slightly positive surface charge of the MNPs) and were gradually internalized by them with a maximum accumulation after 24 h of co-incubation. Wherein, 2 h of MNP co-cultivation with cells resulted in NP localization both on the plasma membrane and inside the cells. It is known that MNPs enter into endosomes after uptake and can further fuse with lysosomes, forming endolysosomes [43,44]. Further, there are several possible scenarios for the development of the events. In one case, internalized NPs can undergo degradation by endolysosomal enzymes; contrariwise, MNPs are known to escape endosomes after internalization and accumulate in the cell cytoplasm, bypassing the degradation [45,46]. Since we found MNP conglomerates inside single-membrane vesicles and directly in the cell cytoplasm, it can be concluded that the synthesized magnetite–gold MNPs escaped from the vesicle compartment after uptake, similar to the NPs demonstrated in [47]. The observation also confirmed that only single MNPs-Cy5 were co-localized with LAMP1-positive vesicles, or endolysosomes. Later, some MNPs could be surrounded by double-membrane vacuoles, or autophagosomes [45]. Thus, starting from 2 h of cell incubation with the MNPs, three main variants of NP localization were found: (1) on the plasma membrane, (2) inside vesicles, and (3) free in the cell cytoplasm.

The research of MNP behavior inside the cells under low-frequency magnetic field exposure demonstrated different types of NP movements: rotational, oscillatory, and indistinguishable. We hypothesize that this could be due to the abundance of various proteins and organelles in the cell cytoplasm that impede such motions. It is known that in physiological conditions, the "protein corona" formed on the surface of NPs can affect their common characteristics (such as size, colloidal stability, and potential) as well as magnetic properties in some cases [48,49]. Moreover, the non-controlled method of MNP aggregation after contact with the cells differs from the process of aggregation in the cell medium and can affect the MNPs' magnetic properties by itself [50]. Finally, in our experiments, the MNPs could interact with the cell cytoskeleton, creating additional resistance to the magnetic field. Indirect evidence of such an interaction can be the directed movement of the MNP conglomerate along the cell, as shown in Video S8. The opportunity for gold NPs to bind with microtubules was demonstrated by Ghalandari et al. [51]. Thus, despite MNP localization in the cell cytoplasm or inside the vesicles, they retained magnetic properties

even a day after internalization and could respond to a magnetic field. However, such a response was predominantly weaker than in the culture medium or water. This, in turn, can reduce the efficiency of the magneto-mechanical effect provided by synthesized magnetite–gold NPs. Further investigations should be conducted to establish the relationship between the MNPs' surface coating and their impact on cell viability under low-frequency magnetic field application.

Based on the obtained results and the data of other researchers, the time point of 3 h of cell co-incubation with MNPs under pulsed low-frequency magnetic field exposure (f = 31 Hz, B = 175 mT, 30 s pulse/30 s pause) [13] was investigated for the magneto-mechanical effect assay. At this moment, MNPs are localized both on the cell plasma membrane and inside the cell, as explained in the Results section. Therefore, it is possible to assess their impact on all compartments.

Before evaluating the in vitro cell viability after magnetic field exposure, we also performed some calculations for a force range over which MNPs-Cy5 can generate and affect the state of a cell membrane. According to the magnetization curves (Figure 1d,e), at 175 mT field B, the magnetization of MNPs (M_B) is 53 $Am^2\ kg^{-1}$. The density ρ of Fe_3O_4 in MNPs is 5200 $kg\ m^{-3}$, and the average MNP radius R is 10.5 nm according to the TEM data. Given the spherical shape of the MNP, its volume is equal to $4/3\pi * R^3$. Then, the average magnetic moment per MNP (m_{MNP}) can be calculated as follows [52]:

$$m_{MNP} = M_B * \rho * \frac{4\pi R^3}{3} = 53\ \mathrm{Am^2\ kg^{-1}} * 5200\ \mathrm{kg\ m^{-3}} * \frac{4\pi(10.5 * 10^{-9}\mathrm{m})^3}{3} = 1.34 * 10^{-18}\mathrm{Am^2}$$

The maximum magnetic torque L_m that can be achieved with these MNPs is when the angle α between the field direction and the magnetic moment of the MNP is 90° ($\sin\alpha = 1$). In this case, the torque is equal to:

$$L_m = m_{MNP} * B = 1.34 * 10^{-18}\mathrm{Am^2} * 0.175\ \mathrm{T} = 2.34 * 10^{-19}\ \mathrm{Nm} = 234\ \mathrm{pN\ nm}$$

Let us assume the situation when the MNPs are located directly on the cell membrane and exhibit the shear/pulling force F_M on it when applying a magnetic field. The distance between the membrane surface and the center of the MNPs is equal to the MNP radius. It means that the force F_M can be calculated as:

$$F_M = \frac{L_m}{R_{MNP}} = \frac{234\ \mathrm{pN\ nm}}{10.5\ \mathrm{nm}} = 22.3\ \mathrm{pN}$$

It is known that forces in the range of ~100 pN are necessary for a cell membrane rupture [11]. According to our estimations above, the forces that individual MNPs can generate are of ~tens pN order of magnitude as well. Moreover, the solutions of MNPs-Cy5 we add to the cells already contained conglomerates of particles (cf. DLS data), and the cells were pre-assembling MNPs-Cy5 into aggregates before the phagocytosis (cf. Figure 5). Thus, the effective forces that can be generated by MNPs located at the cell membrane in our in vitro experiment might be even higher, especially close to the saturation regime. There, the magnetic moment of an MNP conglomerate is proportional to the magnetic moments of the individual particles multiplied by their number.

Our data demonstrated that the magneto-mechanical effect of MNPs causing tumor cell death was achieved only for LNCaP cells at NP concentrations $\geq$70 $\mu g\ mL^{-1}$ Fe_3O_4, but not for the PC-3 cells. The combination of the estimated magnetic moment of an individual MNP (22.3 pN) and the concentration used is in line with other studies on magneto-mechanical cancer cell destruction [16]. Thus, we suggest that such a difference in LNCaP and PC-3 cell response can be due to the different endocytic activity of the corresponding cell lines. Because it was shown above that LNCaP cells interacted and internalized MNPs-Cy5 more often than PC-3 cells, the number of NPs on the plasma membrane and inside the cytoplasm of PC-3 cells could be insufficient to cause any disruption of the components of the cell and the system as a whole. Another reason may be in the difference between

the two investigated cell lines in the internalized MNP behavior under magnetic field exposure. MNPs inside the PC-3 cells did not form small chains and rotated more weakly under the rotation magnetic field application. Based on the morphological features of the cells, the explanation for such an observation can be that the cytoplasm of the PC-3 cells has a higher viscosity due to the enrichment of specific proteins, cytoskeleton reorganization, or a greater vesicle concentration. Moreover, since PC-3 cells are a more aggressive form of prostatic adenocarcinoma than LNCaP cells [53], they can be more resistant to external impacts. Finally, there is a study comparing the resistance of LNCaP and PC-3 cells to fluid shear stress [54]. There, the authors showed that at the stress pulse value of 3950 dyn cm^{-2} (395 Pa), the viability of the PC-3 cell line was higher than that of the LNCaP line. To compare this value to our system, we can assume the force F_M from one MNP (22.3 pN) acting on the cell membrane area equal to the cross-sectional area S of an MNP conglomerate with a diameter d of 251 nm (DLS data). The latter can be calculated as $S = 4\pi(d/2)^2 = 5*10^{-14}$ m^2. Thus, the stress is equal to $F_M/S = 450$ Pa, which is in line with the data from [54].

Thus, the investigated magnetite–gold MNPs represent a prospective multifunctional platform for tumor diagnostics and therapy. Previously, they were shown: (1) to be used as a contrast agent for MRI; (2) to induce controlled magnetic hyperthermia; (3) to deliver drugs to a tumor site; and (4) to be modified with specific vectors, increasing their targeted delivery. In this article, we continued researching the possibility of the application of these MNPs in biomedicine. The behavior of the MNPs under low-frequency magnetic field exposure in water solution in real time and inside tumor cells was demonstrated. The MNP interaction, uptake, and localization inside the cells were observed in detail. Moreover, we established the ability to use the magnetite–gold MNPs for tumor cell death activation mediated by a magneto-mechanical effect. Further research on various magnetic field parameters and cultivation conditions could enhance the effectiveness of the magneto-mechanical effect provided by these NPs.

Supplementary Materials: The following are available online at https://www.mdpi.com/article/10.3390/magnetochemistry8120185/s1.

Author Contributions: Conceptualization, A.A.F., Y.E.K., A.G.S. and M.A.A.; methodology, A.S.G., M.V.E., E.V.L., I.I.K., A.S.E. and P.V.G.; software, O.A.Z. and O.S.S.; validation, I.B.A., R.E.U., V.N.A. and I.V.S.; formal analysis, A.S.G., M.V.E. and A.E.M.; investigation, A.S.G., M.V.E., A.E.M., E.V.L., N.S.V., O.A.Z., I.V.S., A.S.E. and P.V.G.; resources, A.S.G., I.I.K., A.A.F., Y.E.K., A.G.S. and M.A.A.; data curation, M.A.A.; writing—original draft preparation, A.S.G. and M.V.E.; writing—review and editing, E.V.L., O.A.Z., O.S.S., I.B.A., R.E.U., V.N.A. and M.A.A.; visualization, A.S.G., M.V.E., A.E.M., E.V.L., O.A.Z., O.S.S. and I.V.S.; supervision, I.I.K., A.A.F., Y.E.K. and A.G.S.; project administration, A.S.E., P.V.G. and M.A.A.; funding acquisition, A.S.G. and M.A.A. All authors have read and agreed to the published version of the manuscript.

Funding: This research was funded by Russian Science Foundation, grant number 21-74-20077. SSCM investigations were supported by Russian Science Foundation, grant number 22-19-00824.

Institutional Review Board Statement: Not applicable.

Informed Consent Statement: Not applicable.

Data Availability Statement: Not applicable.

Acknowledgments: TEM and confocal imaging were performed on the equipment provided by the MSU Development program (PNR 5.13) and Nikon Center of Excellence at Belozersky Institute of Physico-chemical biology.

Conflicts of Interest: The authors declare no conflict of interest.

References

1. Avasthi, A.; Caro, C.; Pozo-Torres, E.; Leal, M.P.; García-Martín, M.L. Magnetic Nanoparticles as MRI Contrast Agents. *Top. Curr. Chem.* **2020**, *378*, 40. [CrossRef] [PubMed]
2. Wang, Y.; Li, X.; Chen, P.; Dong, Y.; Liang, G.; Yu, Y. Enzyme-instructed self-aggregation of Fe_3O_4 nanoparticles for enhanced MRI T_2 imaging and photothermal therapy of tumors. *Nanoscale* **2020**, *3*, 1886–1893. [CrossRef] [PubMed]
3. Raouf, I.; Khalid, S.; Khan, A.; Lee, J.; Kim, H.S.; Kim, M.-H. A Review on Numerical Modeling for Magnetic Nanoparticle Hyperthermia: Progress and Challenges. *J. Therm. Biol.* **2020**, *91*, 102644. [CrossRef] [PubMed]
4. Frenea-Robin, M.; Marchalot, J. Basic Principles and Recent Advances in Magnetic Cell Separation. *Magnetochemistry* **2022**, *8*, 11. [CrossRef]
5. Chun, S.H.; Yuk, J.S.; Um, S.H. Regulation of cellular gene expression by nanomaterials. *Nano Converg.* **2018**, *5*, 34. [CrossRef]
6. Price, P.M.; Mahmoud, W.E.; Al-Ghamdi, A.A.; Bronstein, L.M. Magnetic Drug Delivery: Where the Field Is Going. *Front. Chem.* **2018**, *6*, 619. [CrossRef]
7. Liu, J.F.; Jang, B.; Issadore, D.; Tsourkas, A. Use of magnetic fields and nanoparticles to trigger drug release and improve tumor targeting. *Wiley Interdiscip. Rev. Nanomed. Nanobiotechnol.* **2019**, *11*, e1571. [CrossRef]
8. Lopez, S.; Hallali, N.; Lalatonne, Y.; Hillion, A.; Antunes, J.C.; Serhan, N.; Clerc, P.; Fourmy, D.; Motte, L.; Carrey, J.; et al. Magneto-mechanical destruction of cancer-associated fibroblasts using ultra-small iron oxide nanoparticles and low frequency rotating magnetic fields. *Nanoscale Adv.* **2022**, *4*, 421–436. [CrossRef]
9. Nikitin, A.A.; Ivanova, A.V.; Semkina, A.S.; Lazareva, P.A.; Abakumov, M.A. Magneto-Mechanical Approach in Biomedicine: Benefits, Challenges, and Future Perspectives. *Int. J. Mol. Sci.* **2022**, *23*, 11134. [CrossRef]
10. Tzoneva, R.; Tsiapla, A.-R.; Uzunova, V.; Stoyanova, T.; Samaras, T.; Angelakeris, M.; Kalogirou, O. Synergistic Effect of Combined Treatment with Magnetic Hyperthermia and Magneto-Mechanical Stress of Breast Cancer Cells. *Magnetochemistry* **2022**, *8*, 117. [CrossRef]
11. Wong, D.W.; Gan, W.L.; Teo, Y.K.; Lew, W.S. Interplay of cell death signaling pathways mediated by alternating magnetic field gradient. *Cell Death Discov.* **2018**, *4*, 49. [CrossRef] [PubMed]
12. Orel, V.E.; Dasyukevich, O.; Rykhalskyi, O.; Orel, V.B.; Burlaka, A.; Virko, S. Magneto-mechanical effects of magnetite nanoparticles on Walker-256 carcinosarcoma heterogeneity, redox state and growth modulated by an inhomogeneous stationary magnetic field. *JMMM* **2021**, *538*, 168314. [CrossRef]
13. Tsiapla, A.-R.; Uzunova, V.; Oreshkova, T.; Angelakeris, M.; Samaras, T.; Kalogirou, O.; Tzoneva, R. Cell Behavioral Changes after the Application of Magneto-Mechanical Activation to Normal and Cancer Cells. *Magnetochemistry* **2022**, *8*, 21. [CrossRef]
14. Li, W.; Liu, Y.; Qian, Z.; Yang, Y. Evaluation of Tumor Treatment of Magnetic Nanoparticles Driven by Extremely Low Frequency Magnetic Field. *Sci. Rep.* **2017**, *7*, 46287. [CrossRef] [PubMed]
15. Master, A.M.; Williams, P.N.; Pothayee, N.; Zhang, R.; Vishwasrao, H.M.; Golovin, Y.I.; Riffle, J.S.; Sokolsky, M.; Kabanov, A.V. Remote Actuation of Magnetic Nanoparticles for Cancer Cell Selective Treatment Through Cytoskeletal Disruption. *Sci. Rep.* **2016**, *6*, 33560. [CrossRef]
16. Wong, D.W.; Gan, W.L.; Liu, N.; Lew, W.S. Magneto-actuated cell apoptosis by biaxial pulsed magnetic field. *Sci. Rep.* **2017**, *7*, 10919. [CrossRef]
17. Chiriac, H.; Radu, E.; Țibu, M.; Stoian, G.; Ababei, G.; Lăbușcă, L.; Herea, D.-D.; Lupu, N. Fe-Cr-Nb-B ferromagnetic particles with shape anisotropy for cancer cell destruction by magneto-mechanical actuation. *Sci. Rep.* **2018**, *8*, 11538. [CrossRef]
18. Alieva, I.; Kireev, I.; Rakhmanina, A.; Garanina, A.; Strelkova, O.; Zhironkina, O.; Cherepaninets, V.; Davydov, V.; Khabashesku, V.; Agafonov, V.; et al. Magnetinduced behavior of iron carbide (Fe7C3@C) nanoparticles in the cytoplasm of living cells. *Nanosyst. Phys. Chem. Math.* **2016**, *7*, 158160.
19. Shen, Y.; Wu, C.; Uyeda, T.Q.P.; Plaza, G.R.; Liu, B.; Han, Y.; Lesniak, M.S.; Cheng, Y. Elongated Nanoparticle Aggregates in Cancer Cells for Mechanical Destruction with Low Frequency Rotating Magnetic Field. *Theranostics* **2017**, *7*, 1735–1748. [CrossRef]
20. Garanina, A.S.; Kireev, I.I.; Zhironkina, O.A.; Strelkova, O.S.; Shakhov, A.; Alieva, I.B.; Davydov, V.A.; Murugesan, S.; Khabashesku, V.N.; Majouga, A.G.; et al. Long-term live cells observation of internalized fluorescent Fe@C nanoparticles in constant magnetic field. *J. Nanobiotechnol.* **2019**, *17*, 27. [CrossRef]
21. Naud, C.; Thébault, C.; Carrière, M.; Hou, Y.; Morel, R.; Berger, F.; Diény, B.; Joisten, H. Cancer treatment by magneto-mechanical effect of particles, a review. *Nanoscale Adv.* **2020**, *2*, 3632–3655. [CrossRef] [PubMed]
22. Zhang, E.; Kircher, M.F.; Koch, M.; Eliasson, L.; Goldberg, S.N.; Renström, E. Dynamic magnetic fields remote-control apoptosis via nanoparticle rotation. *ACS Nano* **2014**, *8*, 3192–3201. [CrossRef] [PubMed]
23. Vegerhof, A.; Barnoy, E.A.; Motiei, M.; Malka, D.; Danan, Y.; Zalevsky, Z.; Popovtzer, R. Targeted magnetic nanoparticles for mechanical lysis of tumor cells by low-amplitude alternating magnetic field. *Materials* **2016**, *9*, 943. [CrossRef]
24. Efremova, M.V.; Naumenko, V.A.; Spasova, M.; Garanina, A.S.; Abakumov, M.A.; Blokhina, A.D.; Melnikov, P.A.; Prelovskaya, A.O.; Heidelmann, M.; Li, Z.-A.; et al. Magnetite-Gold nanohybrids as ideal all-in-one platforms for theranostics. *Sci. Rep.* **2018**, *8*, 11295. [CrossRef]
25. Efremova, M.V.; Nalench, Y.A.; Myrovali, E.; Garanina, A.S.; Grebennikov, I.S.; Gifer, P.K.; Abakumov, M.A.; Spasova, M.; Angelakeris, M.; Savchenko, A.G.; et al. Size-selected Fe_3O_4–Au hybrid nanoparticles for improved magnetism-based theranostics. *Beilstein J. Nanotechnol.* **2018**, *9*, 2684–2699. [CrossRef] [PubMed]

26. Machulkin, A.E.; Garanina, A.S.; Zhironkina, O.A.; Beloglazkina, E.K.; Zyk, N.V.; Savchenko, A.G.; Kotelyanskii, V.E.; Mazhuga, A.G. Nanohybride Materials Based on Magnetite-Gold Nanoparticles for Diagnostics of Prostate Cancer: Synthesis and In Vitro Testing. *Bull. Exp. Biol. Med.* **2016**, *161*, 706–710. [CrossRef] [PubMed]
27. Yu, H.; Chen, M.; Rice, P.M.; Wang, S.X.; White, R.L.; Sun, S. Dumbbell-like bifunctional Au-Fe_3O_4 nanoparticles. *Nano Lett.* **2005**, *5*, 379–382. [CrossRef]
28. Romodina, M.N.; Lyubin, E.V.; Fedyanin, A.A. Detection of Brownian Torque in a Magnetically-Driven Rotating Microsystem. *Sci. Rep.* **2016**, *6*, 21212. [CrossRef]
29. Vavaev, E.S.; Novoselova, M.; Shchelkunov, N.M.; German, S.; Komlev, A.S.; Mokrousov, M.D.; Zelepukin, I.V.; Burov, A.M.; Khlebtsov, B.N.; Lyubin, E.V.; et al. $CaCO_3$ Nanoparticles Coated with Alternating Layers of Poly-L-Arginine Hydrochloride and Fe_3O_4 Nanoparticles as Navigable Drug Carriers and Hyperthermia Agents. *ACS Appl. Nano Mater.* **2022**, *5*, 2994–3006. [CrossRef]
30. Korchev, Y.E.; Bashford, C.L.; Milovanovic, M.; Vodyanoy, I.; Lab, M.J. Scanning ion conductance microscopy of living cells. *Biophys. J.* **1997**, *73*, 653–658. [CrossRef]
31. Korchev, Y.E.; Milovanovic, M.; Bashford, C.L.; Bennett, D.C.; Sviderskaya, E.V.; Vodyanoy, I.; Lab, M.J. Specialized scanning ion-conductance microscope for imaging of living cells. *J. Microsc.* **1997**, *188*, 17–23. [CrossRef] [PubMed]
32. Gorelik, J.; Shevchuk, A.; Ramalho, M.; Elliott, M.; Lei, C.; Higgins, C.F.; Lab, M.J.; Klenerman, D.; Krauzewicz, N.; Korchev, Y. Scanning surface confocal microscopy for simultaneous topographical and fluorescence imaging: Application to single virus-like particle entry into a cell. *PNAS* **2002**, *99*, 16018–16023. [CrossRef] [PubMed]
33. Salikhov, S.V.; Savchenko, A.G.; Grebennikov, I.S.; Yurtov, E.V. Phase composition and structure of iron oxide nanopowders prepared by chemical means. *Bull. Russ. Acad. Sci. Phys.* **2015**, *79*, 1106–1112. [CrossRef]
34. van de Walle, A.; Perez, J.E.; Abou-Hassan, A.; Hémadi, M.; Luciani, N.; Wilhelm, C. Magnetic nanoparticles in regenerative medicine: What of their fate and impact in stem cells? *Mater. Today Nano* **2020**, *11*, 100084. [CrossRef]
35. Gribanovsky, S.L.; Zhigachev, A.O.; Golovin, D.Y.; Golovin, Y.I.; Klyachko, N.L. Mechanisms and conditions for mechanical activation of magnetic nanoparticles by external magnetic field for biomedical applications. *JMMM* **2022**, *553*, 169278. [CrossRef]
36. Wu, J.; Ning, P.; Gao, R.; Feng, O.; Shen, Y.; Zhang, Y.; Li, Y.; Xu, C.; Qin, Y.; Plaza, G.R.; et al. Programmable ROS-Mediated Cancer Therapy via Magneto-Inductions. *Adv. Sci.* **2020**, *7*, 1902933. [CrossRef]
37. Guo, Y.; Yang, W.; Pu, G.; Zhu, C.; Zhu, Y.; Li, J.; Huang, Y.; Wang, B.; Chu, M. Low frequency vibrating magnetic field-triggered magnetic microspheres with a nanoflagellum-like surface for cancer therapy. *J. Nanobiotechnol.* **2022**, *20*, 316. [CrossRef]
38. Sanavio, B.; Stellacci, F. Recent Advances in the Synthesis and Applications of Multimodal Gold-Iron Nanoparticles. *Curr. Med. Chem.* **2017**, *24*, 497–511. [CrossRef]
39. Fantechi, E.; Innocenti, C.; Bertoni, G.; Sangregorio, C.; Pineider, F. Modulation of the magnetic properties of gold-spinel ferrite heterostructured nanocrystals. *Nano Res.* **2020**, *13*, 785–794. [CrossRef]
40. Elmi, G.R.; Saleem, K.; Baig, M.M.F.A.; Aamir, M.N.; Wang, M.; Gao, X.; Abbas, M.; Rehman, M.U. Recent Advances of Magnetic Gold Hybrids and Nanocomposites, and Their Potential Biological Applications. *Magnetochemistry* **2022**, *8*, 38. [CrossRef]
41. Rajkumar, S.; Prabaharan, M. Theranostics Based on Iron Oxide and Gold Nanoparticles for Imaging-Guided Photothermal and Photodynamic Therapy of Cancer. *Curr. Top. Med. Chem.* **2017**, *17*, 1858–1871. [CrossRef] [PubMed]
42. Muzzi, B.; Albino, M.; Gabbani, A.; Omelyanchik, A.; Kozenkova, E.; Petrecca, M.; Innocenti, C.; Balica, E.; Lavacchi, A.; Scavone, F.; et al. Star-Shaped Magnetic-Plasmonic Au@Fe3O4 Nano-Heterostructures for Photothermal Therapy. *ACS Appl. Mater. Interfaces* **2022**, *14*, 29087–29098. [CrossRef] [PubMed]
43. Rathore, B.; Sunwoo, K.; Jangili, P.; Kim, J.; Kim, J.H.; Huang, M.; Xiong, J.; Sharma, A.; Yang, Z.; Qu, J.; et al. Nanomaterial designing strategies related to cell lysosome and their biomedical applications: A review. *Biomaterials* **2019**, *211*, 25–47. [CrossRef] [PubMed]
44. Uzhytchak, M.; Smolková, B.; Lunova, M.; Jirsa, M.; Frtús, A.; Kubinová, Š.; Dejneka, A.; Lunov, O. Iron Oxide Nanoparticle-Induced Autophagic Flux Is Regulated by Interplay between p53-mTOR Axis and Bcl-2 Signaling in Hepatic Cells. *Cells* **2020**, *9*, 1015. [CrossRef] [PubMed]
45. Foroozandeh, P.; Aziz, A.A. Insight into Cellular Uptake and Intracellular Trafficking of Nanoparticles. *Nanoscale Res. Lett.* **2018**, *13*, 339. [CrossRef] [PubMed]
46. Portilla, Y.; Mulens-Arias, V.; Paradela, A.; Ramos-Fernández, A.; Pérez-Yagüe, S.; Morales, M.P.; Barber, D.F. The surface coating of iron oxide nanoparticles drives their intracellular trafficking and degradation in endolysosomes differently depending on the cell type. *Biomaterials* **2022**, *281*, 121365. [CrossRef] [PubMed]
47. Alieva, I.B.; Kireev, I.; Garanina, A.S.; Alyabyeva, N.; Ruyter, A.; Strelkova, O.S.; Zhironkina, O.A.; Cherepaninets, V.D.; Majouga, A.G.; Davydov, V.A.; et al. Magnetocontrollability of Fe_7C_3@C superparamagnetic nanoparticles in living cells. *J. Nanobiotechnol.* **2016**, *14*, 67. [CrossRef]
48. Jiang, W.; Lai, K.; Wu, Y.; Gu, Z. Protein corona on magnetite nanoparticles and internalizationof nanoparticle–protein complexes into healthy and cancer cells. *Arch. Pharmacal Res.* **2014**, *37*, 129–141. [CrossRef]
49. Vogt, C.; Pernemalm, M.; Kohonen, P.; Laurent, S.; Hultenby, K.; Vahter, M.; Lehtiö, J.; Toprak, M.S.; Fadeel, B. Proteomics Analysis Reveals Distinct Corona Composition on Magnetic Nanoparticles with Different Surface Coatings: Implications for Interactions with Primary Human Macrophages. *PLoS ONE* **2015**, *10*, e0129008. [CrossRef]

50. Brollo, M.E.F.; Flores, P.H.; Gutierrez, L.; Johansson, C.; Barber, D.F.; Morales, M.P. Magnetic properties of nanoparticles as a function of their spatial distribution on liposomes and cells. *Phys. Chem. Chem. Phys.* **2018**, *20*, 17829–17838. [CrossRef]
51. Ghalandari, B.; Asadollahi, K.; Shakerizadeh, A.; Komeili, A.; Riazi, G.; Kamrava, S.K.; Attaran, N. Microtubule network as a potential candidate for targeting by gold nanoparticle-assisted photothermal therapy. *J. Photochem. Photobiol. B* **2019**, *192*, 131–140. [CrossRef] [PubMed]
52. Nikitin, A.A.; Yurenya, A.Y.; Zatsepin, T.S.; Aparin, I.O.; Chekhonin, V.P.; Majouga, A.G.; Farle, M.; Wiedwald, U.; Abakumov, M.A. Magnetic Nanoparticles as a Tool for Remote DNA Manipulations at a Single-Molecule Level. *ACS Appl. Mater. Interfaces* **2021**, *13*, 14458–14469. [CrossRef] [PubMed]
53. Tai, S.; Sun, Y.; Squires, J.M.; Zhang, H.; Oh, W.K.; Liang, C.-Z.; Huang, J. PC3 is a cell line characteristic of prostatic small cell carcinoma. *Prostate* **2011**, *71*, 1668–1679. [CrossRef] [PubMed]
54. Hope, J.M.; Bersi, M.R.; Dombroski, J.A.; Clinch, A.B.; Pereles, R.S.; Merryman, W.D.; King, M.R. Circulating prostate cancer cells have differential resistance to fluid shear stress-induced cell death. *J. Cell Sci.* **2021**, *134*, jcs251470. [CrossRef]